Mechanical Systems and Signal Processing

A hybrid framework for remaining useful life estimation of turbomachine rotor blades
--Manuscript Draft--

Highlights

- A hybrid diagnosis and prognosis framework is presented for mechanical systems.
- The framework uses condition monitoring data, data-driven and physics-based models.
- The framework is applied on turbomachine rotor blades with natural fatigue cracks.
- Blade tip timing and Gaussian process regression are used to infer the crack length.
- An unscented Kalman filter is used to update the crack growth model for prognosis.

A hybrid framework for remaining useful life estimation of turbomachine rotor blades

B. Ellis[*], P.S. Heyns, S. Schmidt

Centre for Asset Integrity Management, University of Pretoria, Pretoria, 0002, South Africa
(brian.ellis@live.co.za[*], stephan.heyns@up.ac.za, stephan.schmidt@up.ac.za)

Abstract

Hybrid methods for prognosis of mechanical components have the potential of improving remaining useful life (RUL) estimations. Hybrid methods combine physics-based and data-driven methods to diagnose faults and predict when failures will occur. In this work, we propose a hybrid framework that estimates the RUL from routine maintenance inspection data and condition monitoring data.

This hybrid framework is applied to turbomachine rotor blades. Blade tip timing (BTT) measurements are used for condition monitoring. The least squares spectral analysis (LSSA) method is used to find the natural frequency. The natural frequency is a function of the blade's health state and is used to infer the crack length in the blade's root. To accommodate for artificial rotational stiffening, an interpolation model of the blade's Campbell diagram, generated from a finite element model, is used.

In the proposed methodology, we use an ensemble physics-based model that serves as a prior probability density function for a Gaussian process regression (GPR) model. The predictive distribution of the GPR model is constructed by conditioning the physics-based model on the observed data from routine maintenance inspections. We also compare this hybrid diagnosis model to the physics-based technique and other data-driven methods. The hybrid diagnosis model outperformed the physics-based method and data-driven methods.

The unscented Kalman filter (UKF) is used to estimate and forecast the evolution of the crack length over time. Paris' law coefficients are used as hidden latent variables in a hybrid degradation model. In the diagnosis and prognosis phases, we use the unscented transform to efficiently approximate the probability density functions of the crack length and the crack growth law parameters.

Finally, we compare the applied hybrid model to a purely physics-based model and show that the hybrid model outperforms the physics-based model in predicting the length of a crack. We demonstrate that the hybrid model increases the accuracy and precision of RUL prediction from physics-based models with 60% on average.

Keywords:

Hybrid remaining useful life methods; Fatigue crack propagation; Unscented transform; Gaussian processes; Unscented Kalman filter; Turbomachinery.

## 1. Introduction

Reliable estimation of *remaining useful life* (RUL) of mechanical components is essential for predictive maintenance strategies as it ensures safety against inadvertent failure and could save significant costs by enabling components to operate well-above their designed life [1], [2]. Yet, there is no generally accepted best way of determining the RUL of a mechanical component from

condition monitoring measurements. Usually, either physics-based methods or data-driven models are used for predicting RUL.

Physics-based models determine RUL from a first principles approach [3]. These models can be constructed prior to collecting any data of the component. However, two sources of error arise when using physics-based models namely (i) modelling errors due to simplifying assumptions and (ii) numerical simulation errors. Hence, physics-based models have unquantifiable uncertainty before any data is collected. *Data-driven models*, on the other hand, use machine learning techniques to determine RUL from recordings of the component's condition over time. Lei et. al [4] postulated that with enough data, a data-driven model will outperform the accuracy of physics-based models. However, the largest drawback of data-driven methods is that it is expensive and impractical to obtain sufficient historical fault [5]. Many identical components need to undergo a complete degradation cycle - from healthy to completely damaged - to have an adequate database for training data-driven models.

It is therefore essential to use methods that can alleviate the shortcomings of physics-based and data-driven methods for machines with limited historical fault data. Liao and Köttig [6] reviewed and categorised various hybrid modelling frameworks for predicting RUL from condition monitoring data. *Hybrid models* refers to combinations of physics and data-driven methods. The purpose of a hybrid prognosis method is to improve the precision and accuracy of the models that estimate (i) the condition and (ii) the RUL of a component. According to Liao and Köttig [6], the sort of hybrid model is determined by the type of data collected and the availability of a physics-based model.

Figure 1 presents a simplification of the procedure proposed in Ref. [6] for calculating the RUL under condition monitoring information. The first part of the framework computes condition indicators from sensor measurements. A diagnosis model relates the condition indicators to the damage, such as crack length, of the component. A damage propagation model then finally predicts the future damage from the estimated future operating conditions [3]. The RUL is determined when the predicted damage exceeds the damage specification limits [7]. These limits are specified at the design stage of the component.
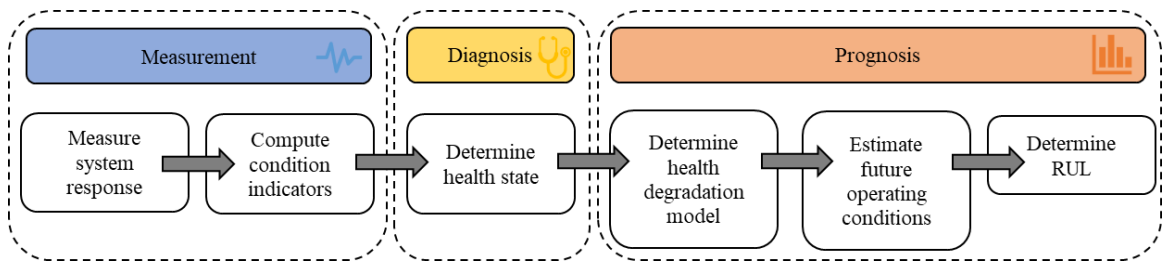
Figure 1: Simplified procedure for determining RUL of components from condition monitoring based on the work in Ref. [6]

Liao and Köttig [6] presented hybrid frameworks for diagnosis and prognosis of Lithium-ion batteries in which the health state is unobservable. The health states in these systems are often inferred from real-time measurements. Many mechanical systems are subject to routine maintenance inspection where recordings of the damage through non-destructive testing (NDT) are made. During these routine NDT inspections diagnostics data is collected. The damage in most mechanical components is only observable during these inspections and therefore hybrid models for mechanical components are different from those proposed by Liao and Köttig [6].

In Figure 2, we propose a novel hybrid framework. This framework applies to mechanical components with routine maintenance inspection data consisting of observable damage parameters. A hybrid diagnosis model is the key difference that distinguishes this model from that

presented by Liao and Köttig [6]. The hybrid property stems from the fact that different model types (physics-based and data-driven) are used within the framework. We refer to the proposed framework as the hybrid-diagnosis-prognosis framework. Notice that two types of data are used in this framework namely NDT data and condition monitoring data. The work is based on the fact that in many mechanical systems, physics-based degradation models are used in the design stage of the component are available before the component is commissioned.
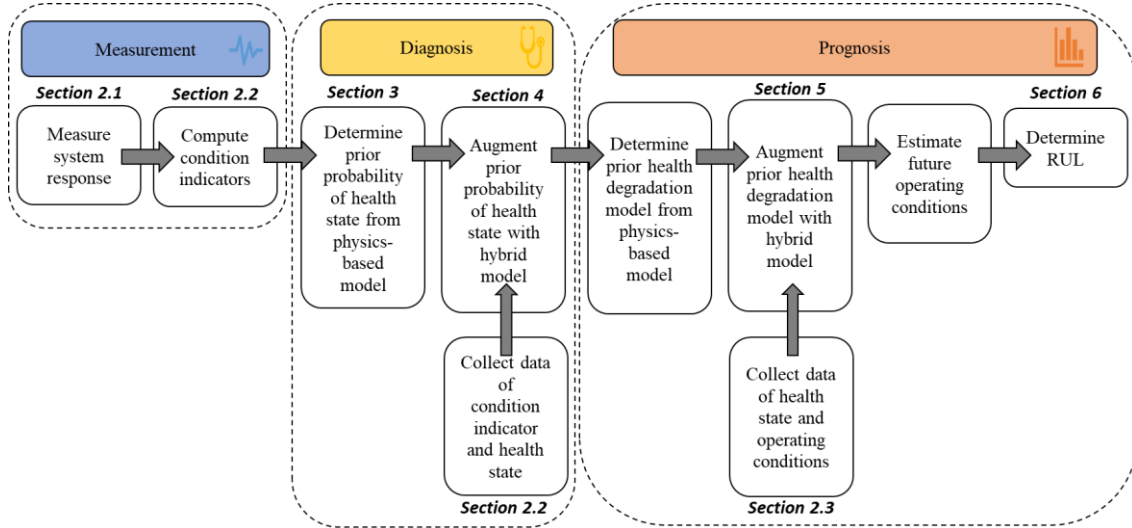
Figure 2: Novel hybrid framework for condition monitoring of mechanical components with partially observable damage states during maintenance inspections.

In this work the proposed general framework is applied on turbomachine rotor blades with root cracks. Turbomachine rotor blades are subject to extreme operating conditions that mainly cause fatigue cracks to initiate and propagate at the root of the blade [8]. Predictive maintenance strategies are essential for these blades since a single blade failure could have catastrophic effects on the entire system.

The contributions of this work are as follows:

- A novel hybrid-diagnosis-prognosis framework is proposed for mechanical systems that are subject to routine NDT inspections.
- We demonstrate the benefits of the proposed method on turbomachine rotor blades using blade tip timing as a condition monitoring technique and show that the method performs much better than data-driven methods and physics-based methods when limited data is available.

The paper is structured as follows: Section 2 presents the experimental test-rig and acquired data that are considered in this work. In Section 3, we construct the physics-based diagnostics model from finite element simulations of the blade. We combine the data and physics models for diagnosis and prognosis in Sections 4 and 5, respectively. For hybrid diagnosis, we employed a Gaussian process regression (GPR) model, and for hybrid prognosis, we used an unscented Kalman filter (UKF). Finally, in Section 6 we predict the RUL and compare the hybrid approach to the physics-based approach.

2. Experimental work

In our work, we investigated the real-time hybrid-diagnostics-prognostics framework by implementing the methodology on a laboratory test rotor with a single NACA 4506 airfoil rotor blade made from Aluminium T6-6082.

The experimental process is shown in Figure 3. The experimental tests were performed in two alternating phases, namely, (i) in situ blade tip timing (BTT) and (ii) accelerated fatigue on a shaker. BTT condition monitoring measurements were acquired from the turbine testbench. Thereafter, the blade was removed from the turbine testbench and mounted on a shaker to accelerate the blade fatigue failure. The BTT and crack growth phases were separated for two reasons:

1. The laboratory test rotor used for the BTT experiments was not capable of generating adequate aerodynamic loads to grow an in-situ crack within a reasonable time.
2. The risk of catastrophic failure becomes too large when growing in-situ cracks. This potential damage to the equipment and the laboratory as well as the potential harm to personnel made the test unacceptable.
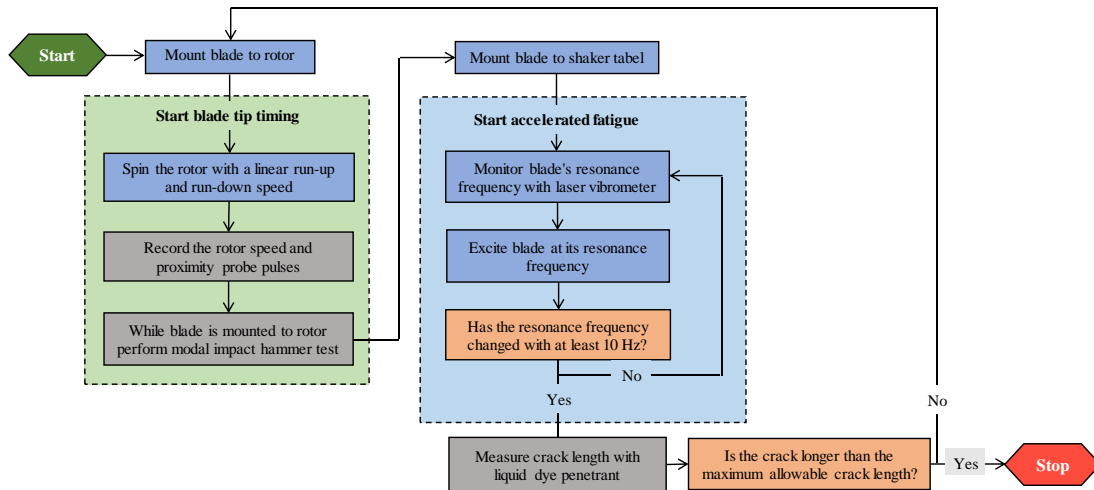
Figure 3: The experiment process flow diagram for testing a single turbomachine blade.

During the accelerated fatigue tests, the shaker applied high amplitude vibrations to the base of the mounted blade. The blade was removed from the shaker table when sufficient damage was induced. The crack length was measured using a liquid dye penetrant test. The crack length measurements were used as NDT inspection data in this work. This investigation made use of ten blades. Each experiment started with a new blade and the BTT and accelerated crack growth phases of the test were successively applied until the blade was excessively damaged. Section 2.1 describes how the BTT readings were processed to obtain the condition indicator of the blade. The two parts of the experimental campaign, blade tip timing measurements and accelerated fatigue tests, are subsequently detailed in Sections 2.2 and 2.3, respectively.

2.1. Blade tip timing (BTT)

The BTT technique, which was used for condition monitoring, is introduced in this section. BTT is a signal processing method for measuring the vibration of turbomachine rotor blades [9]. BTT is one of the preferred condition monitoring methods for turbomachine rotor blades because it measures the displacement of all the blades without interfering with the blade, does not require

cables connected to rotating parts, and saves costs because these sensors can withstand harsh operating conditions [10]. BTT condition monitoring is frequently used to measure a blade's natural frequency, which is very useful for health monitoring applications. The performance of the hybrid methodology is much dependent on the quality of the condition monitoring measurements and the associated signal processing methods [11]. In practical applications of the hybrid methodology, sensors positioned on a blade (e.g., strain gauges with telemetry) cannot be relied upon to provide high quality condition information over time. This emphasizes the importance of BTT as a condition monitoring approach for turbomachine rotor blades.

BTT gauges the instant that a rotor blade tip passes proximity sensors mounted on the hub of the turbomachine. This is referred to as the time of arrival (TOA) and can be used to calculate the vibration of the blade tip relative to its root, assuming that the shaft speed is also accurately measured. Figure 4 illustrates the measurement technique. BTT is an ongoing research field, due to various methods of treating noise and difficulties in analysing event-based signals; research in this field is often divided into two categories namely (i) signal reconstruction and (ii) identification of vibration characteristics [12], [13].
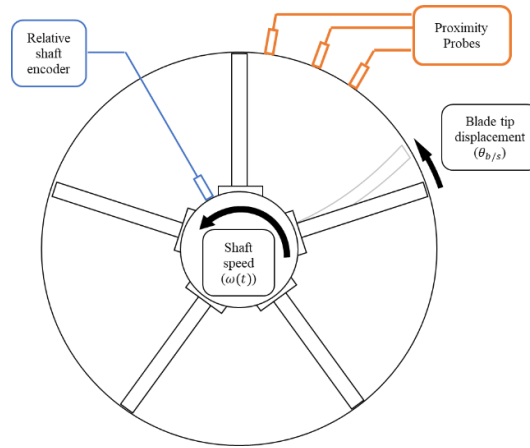
Figure 4: Illustration of the blade tip timing measuring technique with a multiple pulse per revolution (MPR) shaft encoder at the shaft and proximity sensors at the outer hub.

The signal reconstruction step converts to converting the TOA measurements from the proximity sensors to relative displacements of the blade tip. This process usually requires the angular displacement of the shaft measured with a once per revolution (OPR) or multiple pulse per revolution (MPR) tachometer. The recursive solution of the signal reconstruction problem

$$\theta_{b/s}(t_{i+1}) = \Delta\theta_b - \Delta\theta_s + \theta_{b/s}(t_i) = \theta_b(t_{i+1}) - \theta_b(t_i) - \int_{t_i}^{t_{i+1}} \omega_s(\tau)\,d\tau + \theta_{b/s}(t_i) \qquad (1)$$

is derived from the relative dynamics equations as presented by Meriam et. al. [14]. The displacement of the blade tip relative to the rotor shaft, the displacement of the blade tip, the displacement of the shaft and the angular velocity of the shaft are denoted $\theta_{b/s}$, θ_b, θ_s and ω_s respectively and are evaluated at the recorded TOA's, denoted t_i. Note that the formulation of this equation assumes the relative angular displacement of the blade at TOA t_i is known before solving the equation at TOA t_{i+1}. However, $\theta_{b/s}(t_0)$ is often assumed zero since the displacement of the blade tip cannot be calculated at the first TOA unless the rotor is started from rest.

The biggest challenge for accurate signal reconstruction is how signal noise affects the calculated relative displacement. The signal noise either originates from TOA estimation errors or from the

estimation of the function $\omega_s(t)$. Each evaluation of Equation (1) accumulates noise due to $\omega_s(t)$ which is discretely measured from an OPR/MPR tachometer. If the function $\omega_s(t)$ is poorly approximated with an MPR zebra strip encoder that has geometrical errors on the zebra strip, the blade tip displacement is expected to reflect the accumulated noise. Diamond et al. [15] proposed a Bayesian approach to compensate for the geometric errors of simple optical MPR tachometers (e.g. zebra strips), using geometric compensation. The purpose of geometric compensation is to refine the measured angular velocity of the shaft such that a numerical integration of the signal is correctly approximated. In our experiments, we utilize geometric compensation to improve the signal reconstruction from the BTT measurements.

In the vibration characteristic identification step, the resonance frequencies and the blade's vibration amplitudes are estimated from processed BTT signals. The natural frequency of a rotor blade is an important indicator of its health since it is a property of the blade that is invariant to aerodynamic loads and changes predictably with increased rotor speeds owing to artificial rotational stiffening.

As seen from the signal reconstruction problem, the blade displacement is only calculated at a TOA, which implies that the TOA sampling frequency must be a function of (i) the angular velocity, (ii) the number of proximity sensors and (iii) the location of the sensor around the circumference of the hub. This generally results in a varying sampling frequency, which makes Fourier methods such as the discrete Fourier transform unsuitable.

Transient BTT analysis relies on changes in the shaft speed to observe the response of the blade at different frequencies. These analyses are analogous to plotting transmissibility or frequency response functions (FRF) of vibrating systems. The techniques utilise

$$\theta_{b/s}(t) = A\cos(2\pi f t) + B\sin(2\pi f t) + C \tag{2}$$

to model the response of the blade as a function of time and frequency. Regularly, a least squares error regression is fit for different frequencies, denoted f. That is, the model parameters A, B and C are estimated from the reconstructed blade displacement data $\theta_{b/s}$ at selected frequencies. The frequency information is obtained for frequencies that minimise the squared error between the data and equation (2). This least squares approach is also related to the *Lomb-Scargle periodogram* [16]. In a transient BTT analysis, the hyperparameters of the model in Equation (2) (namely A, B and C) are fitted on short-time data which results in a function of both frequency and time. This method is called *least squares spectral analysis* (LSSA); LSSA constructs a time frequency diagram where the maximum amplitude in the diagram represents a resonance frequency of the blade tip.

The natural frequency of the blade tip is not constant during rotation due to centrifugal stiffening. When the blade spins at high angular velocities the centrifugal loads cause the blade to stretch, and the natural frequency consequently increases. This effect can be captured on a Campbell diagram which shows measured resonance frequency lines superimposed on engine order lines. For the blades used in our experiments the natural frequency of the blade $f_{n,\omega}$ can be described by

$$f_{n,\omega} = f_{n,0} + 0.0002(f_s) + 0.0022\,(f_s)^2 \tag{3}$$

where f_s is the shaft speed. Equation (3) was determined from FEM simulations of the rotating blade. Thus, if a resonance shaft speed (denoted f_r) is detected at a known engine order (denoted EO), the natural frequency without artificial stiffening (denoted $f_{n,0}$) can be solved from

$$f_{n,0} = EO\,f_r - 0.0002(f_r) - 0.0022\,(f_r)^2 \tag{4}$$

The importance of finding the natural frequency without artificial stiffening stems from the fact that the natural frequency in a fixed reference frame is determined from data collected while the rotor is spinning.

2.2. Blade tip timing experiments

During our BTT condition monitoring tests, a single blade was mounted on the rotor to reduce the extent of possible damage in the case of inadvertent failure of the damaged blade. The testbench is shown in Figure 5. The rotor setup, proximity probes and tachometer are shown in Figure 6. Counterbalances were added to the rotor to mitigate the presence of rotor imbalance loads. A single pressurised air nozzle was used to discharge high velocity air to excite the blade tip. The aerodynamic loads on the blade tip are not equivalent to those present in typical turbomachines. However, the blade excitation frequency is often observed as an integer multiple of the shaft rotation speed for real turbomachines [17]. This is referred to as synchronous vibration and is a limiting assumption about the response of the blade due to the nature of the aerodynamic loads. Equation (4) assumes synchronous vibration and only requires the resonance speed and the known engine order to evaluate the natural frequency in a stationary reference frame.
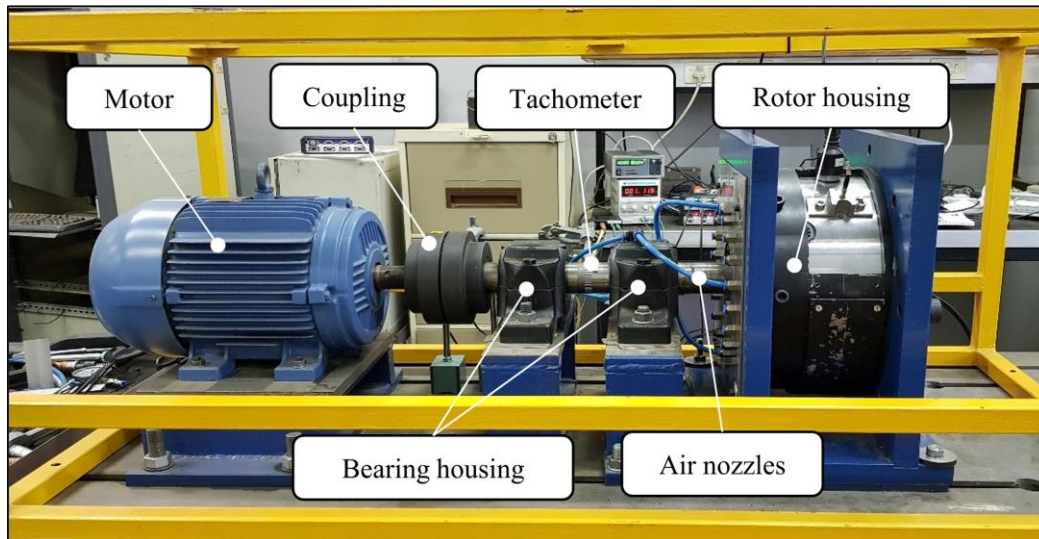
Figure 5: The rotor BTT testbench used to measure the blade tip vibration for the condition monitoring tests.
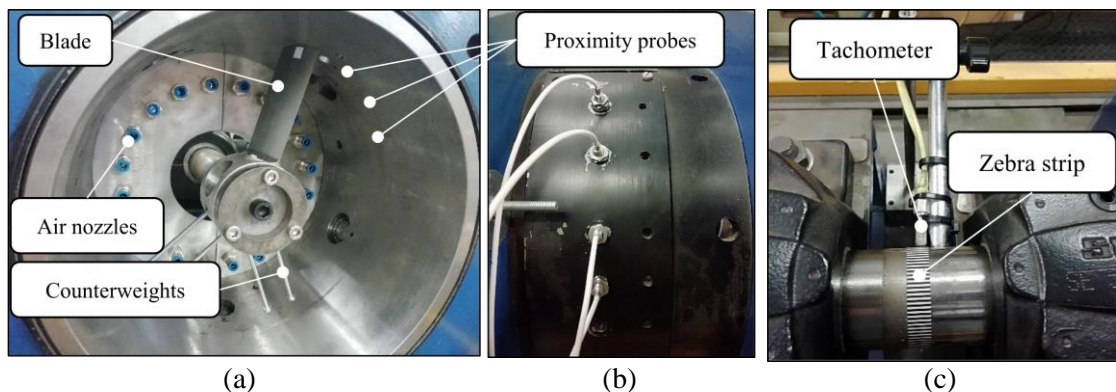
Figure 6: (a) The inside of the rotor housing with a single blade mounted to the rotor shaft, (b) the proximity probes mounted on the outside of the rotor housing and (c) the optical shaft encoder used for measuring the shaft angular speed.

During the BTT tests the rotor angular velocity was changed linearly. The speed of the rotor was swept up and down to determine which speeds caused the blade tip to resonate, which was then used to calculate the natural frequency. For our experiments, we investigated the tenth engine order resonance speed; the tenth engine order is the lowest resonance that was detected for all blades when the rotor speed was swept-up to maximum rotor speed. In practical applications, the relevant engine order for excitation is not necessarily known. This is because the blade excitation frequency is determined by the nature of the aerodynamic loads and the shaft speed. In these cases, it is recommended to find two sequential resonance shaft speeds to solve for the engine orders and natural frequency simultaneously.

Three proximity probes were mounted to the outer hub of the rotor. Figure 7 shows the reconstructed blade displacement signal obtained from a single BTT test and the angular velocity of the shaft, using the method described in Section 2.1. The figure shows the calculated displacements for each probe independently since the blade relative displacement is not known at the first TOA for each proximity probe. The LSSA technique accounts for this assumption by fitting a separate bias constant to the signal from each probe. That is, each probe has its own constant C in the regression model presented in Equation (2) while sharing the other constants A and B. Figure 8 shows a contour graph and waterfall plot of the LSSA method applied to the reconstructed signal. The figure shows that at an angular speed of 20.53 Hz the amplitude of the blade displacement is large. This large amplitude in the blade displacement is a characteristic of the detected resonance rotor speed. The natural frequency of the blade is then calculated from the resonance speed using Equation (4). In this case, the natural frequency was measured as 204.4 Hz. It is emphasised that the natural frequency measured from BTT is estimated in a stationary reference frame, by compensating for the artificial stiffening of the blade during rotation. Equation (4) interpolates the natural frequency line on the Campbell diagram to transform the natural frequency of the rotating blade to the natural frequency of the blade in the stationary reference frame.

(a)

(b)
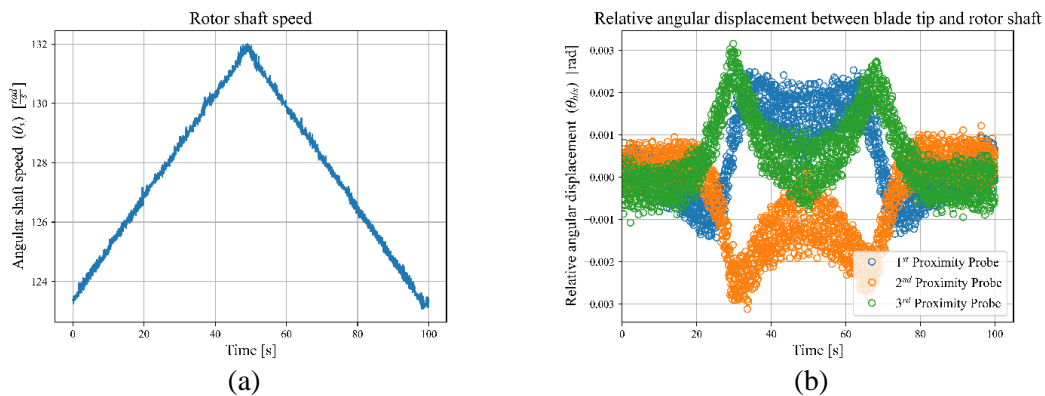
Figure 7: (a) The measured angular shaft speed obtained from the tachometer and (b) the calculated blade tip angular displacement from the three proximity probes for a single BTT experiment.

(a)   (b)
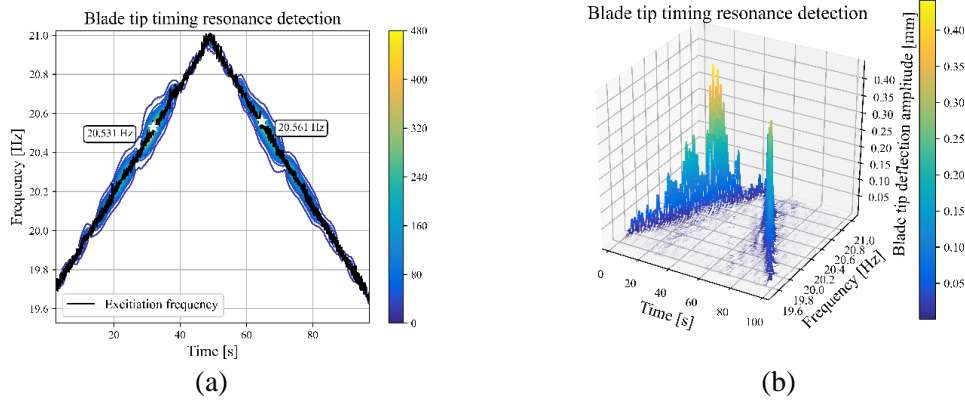
Figure 8: (a) The contour plot and (b) waterfall plot of the LSSA method applied to the calculated blade tip displacement in Figure 5, showing the shaft speeds that cause resonance.

Once the BTT measurements were recorded and the rotor was brought to rest, a modal impact hammer test was conducted. The blade remained mounted to the rotor and the natural frequency of the blade was measured from the frequency response function (FRF) of the blade. Thus, two measurements of the first mode natural frequency were made, namely (i) an estimation using BTT while the rotor is spinning and (ii) a measurement based on the FRF while the rotor is stationary. These two measurements were obtained for all ten blades with multiple crack lengths. All the data collected in these experiments are plotted in Figure 9.
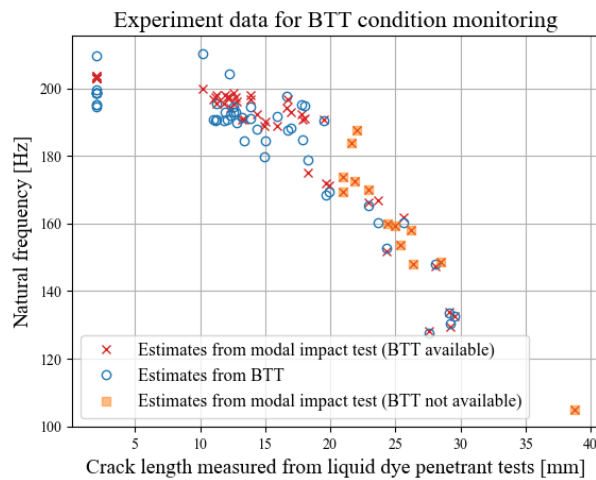
Figure 9: Experimentally collected data from BTT condition monitoring test for diagnosis of turbomachine rotor blades from determined natural frequencies.

Some of the BTT experiments failed to collect enough data to determine the natural frequencies of the blades. This was caused by a failure of the measurement equipment (optical shaft encoder and the proximity probe sensors), which resulted in resonance not being detected in the applied rotor speed range. These points are highlighted in the figure. Notice from the figure that the proposed BTT method approximates the modal impact test measurements for small crack lengths. However, for all crack lengths the deviation between the two measurements was less than 10 Hz.

The BTT-based estimation of the natural frequency was used to further our investigation of hybrid-based models. In practical implementations of turbomachines this type data is collected from regular maintenance interruption to measure lengths of cracks present in the blade.

2.3.　　　　Accelerated fatigue experiments.

The accelerated fatigue tests were implemented to safely grow a crack at the root of the blade. After condition monitoring measurements were acquired for the blade in a specific condition, the blade was removed from the blade tip timing test bench. The blade was rigidly mounted to a slip table that was excited using an electrodynamic shaker. The velocity of the tip of the blade was measured using a laser vibrometer.

Figure 10 (a) and (b) show the blade mounted to the slip table in the same orientation as mounted in the rotor. The recorded velocity response of the blade tip owing to the vibration of the electrodynamic shaker is used to generate a frequency transmissibility function, e.g., a function that plots the amplitude of the vibration magnification as a function of excitation frequency. The resonance frequency of the blade is tracked using the peak of this transmissibility function. A closed feedback control loop kept the blade at resonance, during these experiments, by repeatedly sweeping across a small frequency range to track changes in resonance frequency of the blade. The vibration amplitude of the shaker was automatically controlled to guarantee that the blade tip was not subjected to excessively small and large vibration amplitudes. The blade's resonance frequency was reduced by at least $10\ Hz$ during the accelerated fatigue tests. Figure 10 (c) and (d) show how the crack length is measured from the liquid dye penetrant test; a vernier calliper was used to measure the crack length. The cracks in these blades were not artificially seeded and instead resulted from simply shaking the blade at its resonance frequency.

| (a) | (b) | (c) | (d) |
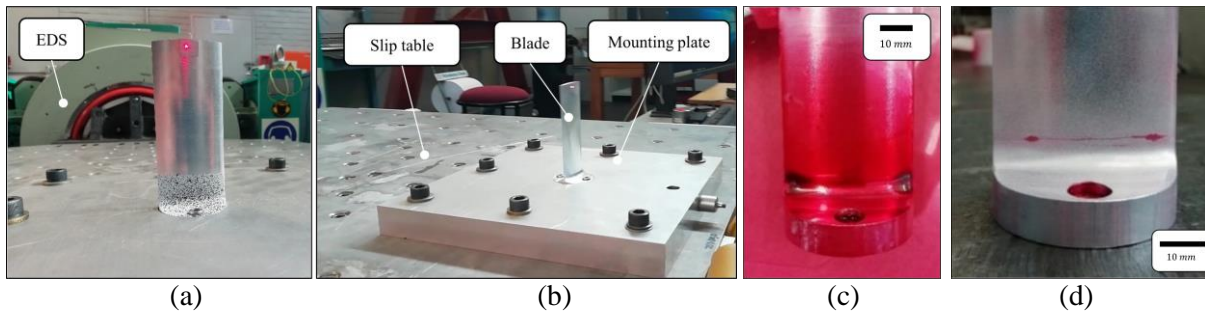
Figure 10: (a) Electrodynamic shaker (EDS) with blade mounted to the table and (b) a side-view. (c) Blade coated with red liquid dye penetrant and (d) a developed NDT result for measuring crack length.

The top frame in Figure 11 (a) shows the measured crack length as a function of the number of cycles for a single blade, namely for blade 1. The mean applied stress intensity factor (SIF) for this blade is shown in the bottom frame. Figure 11 (b) depicts measured crack length as function of the number of loading cycles for the entire set of blades that was tested. For brevity, the stress amplitudes for the other blades are not shown.
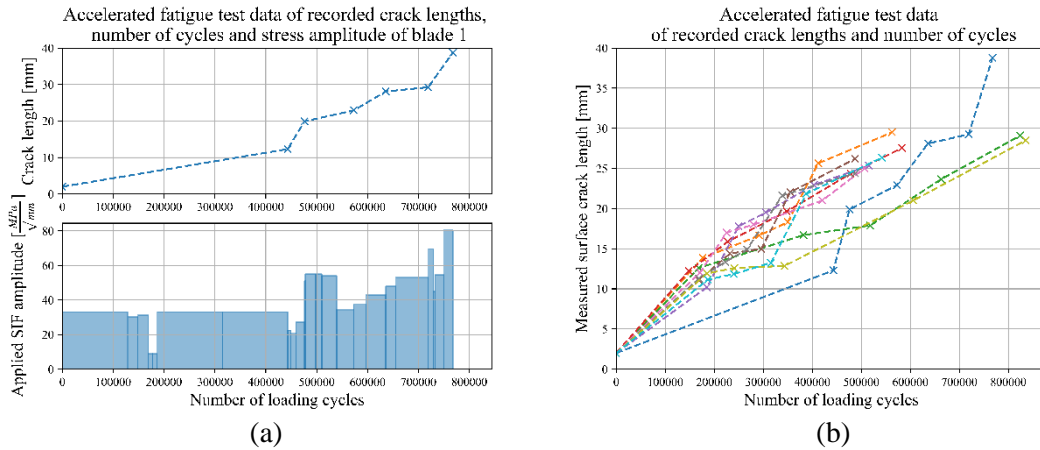
Figure 11: The accelerated fatigue test data (a) for a single blade with the corresponding applied SIF amplitude and (b) the measured crack lengths for all the blades plotted against the number of loading cycles.

3. Physics-based simulations

In this section we present the necessary simulations to model the degradation of the blade using a physics-based approach. These simulations are part of the hybrid diagnosis model and fits in the highlighted portion of Figure 12.
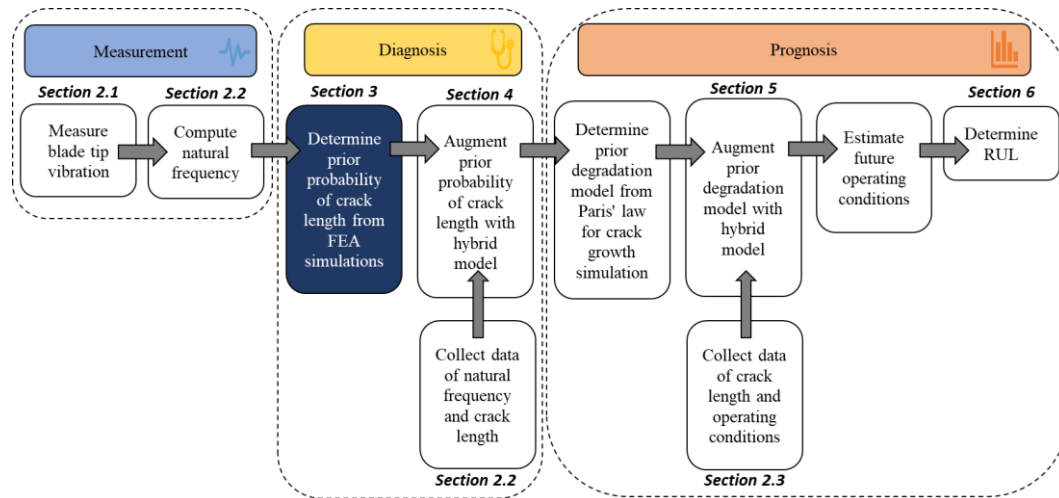
Figure 12: The hybrid framework where the highlighted part shows the physics-based diagnostics model that is constructed in this section.

Two sets of simulations were performed, namely,

(i) an ANSYS separating, morphing and remeshing (SMART) simulation for determining crack size, crack path and the properties of the crack subject to the assumed future operating loads; and

(ii) a set of modal analyses to determine the relationship between the crack length and the first mode natural frequency.

11

3.1.   Simulation 1: Separating, morphing and remeshing fatigue simulation

The physics-based model is used in this work to relate the crack length to the blade's first natural frequency. However, this implies that the crack geometry needs to be defined prior to the modal analysis. The crack geometry is unknown in the actual NACA 4506 airfoil-shaped blade during operation. Therefore, crack growth simulations were performed to identify the geometry of the crack itself, whereafter a modal analysis could be performed to determine the natural frequency of the cracked blade. To account for the uncertainty in the crack initiation and growth in the actual test specific, 10 crack growth simulations were run with various initial crack sizes to estimate the crack geometry and account for the uncertainty in the crack initiation and growth in the actual specimen. The underlying assumptions of these simulations were that (i) the geometry of the crack is approximated as a semi-elliptical surface crack and (ii) the location of the crack is assumed at the location of the maximum bending stress when the blade tip is deflected. All our experimental work had cracks at the same location with no prior seeding of the crack. Admittedly, this assumption is limiting for blades from a different failure mechanism.

More specifically, we consider two methods for determining the crack geometry. The first method is a FEM simulation using ANSYS SMART crack growth to update the geometry of a crack based on the *stress intensity factor* (SIF) at the crack front and Paris' law. Figure 13 (a) and (c) show different stages of the FEM and the associated SIF along the crack contour is shown in Figure 13 (b) and (d). Because most of the contour lines in Figure 13 (b) and (d) are close to each other, the SIF along the crack contour indicates that the mesh surrounding the crack front is fine enough to estimate the properties of the crack. The second method is an approximation method that solves the SIF of a semi-elliptical crack in a rectangular cross-sectional plate using empirical relationships established by Raju and Newman. These equations are well known approximations to cantilever shaped structures and are listed in Refs. [18]–[20]. The length and depth of the crack were numerically updated using Paris' law and a classical finite difference numerical integration scheme.

(a)   (b)

(c)   (d)
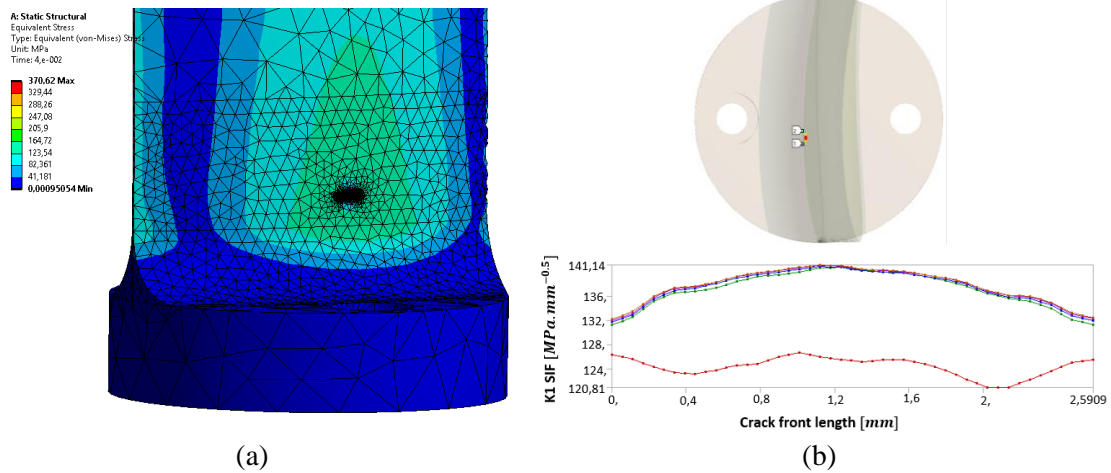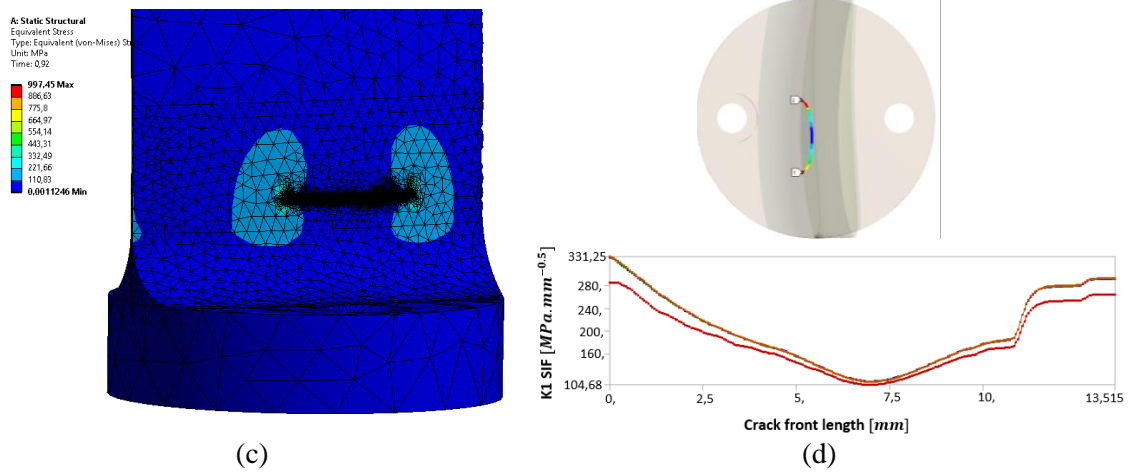
Figure 13: (a) ANSYS smart crack growth simulation mesh with (b) the associated crack geometry and SIF for a small crack and (c) the FEM mesh with (d) the crack geometry and SIF of a large crack.

The length and the depth of the crack are recorded from both methods and are plotted in Figure 14 along with the normalised SIF. Figure 14 (a) shows multiple ANSYS SMART crack growth simulations with cracks of different initial sizes and depths. Note that the dashed horizontal line indicates the thickness of the blade; the Raju-Newman approximation therefore indicates that the crack will break through the thickness of the blade at approximately 17 mm crack length. The FEM simulations fail to simulate cracks close to 17 mm due to a discontinuity in the crack front. A least-squares regression line was fit through both simulation results to approximate the crack depth for larger cracks. Of course, the length of the crack does not determine the depth of the crack; thus, the depth of the crack is an uncertain parameter and contributes to the uncertainty of the natural frequency. We observed from all the crack growth simulations that the depth of the crack may vary with a standard deviation of at least 0.1 mm from the least squares regression fit in Figure 14 (a).

(a)   (b)
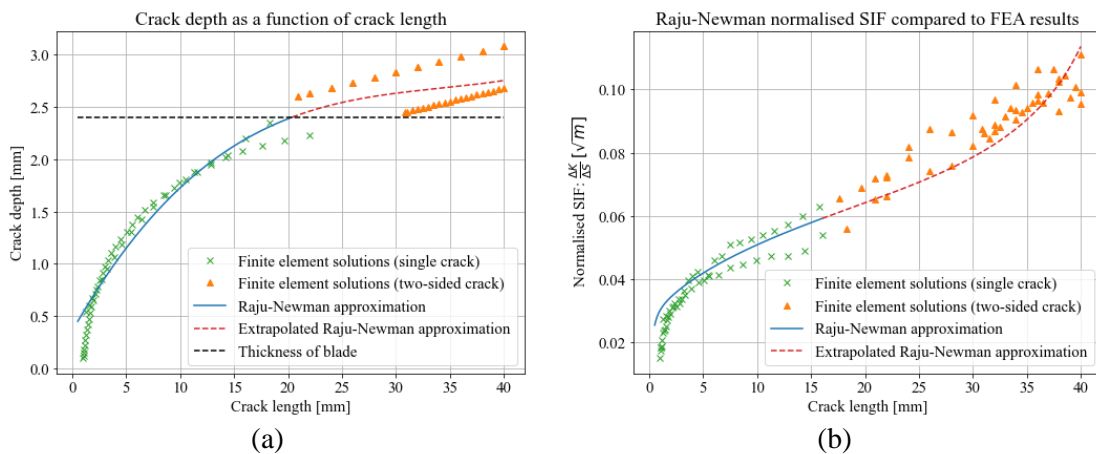
Figure 14: (a) The simulated crack depth versus surface crack length from FEM simulations and approximated Raju-Newman equations and (b) the normalised SIF as a function of crack length.

Figure 14 (b) depicts the solutions to the normalised SIF from both the FEA results and the Raju-Newman approximation equations. The Raju-Newman equations are only applicable for a certain range of crack lengths and are not defined for the region shown in red. However, the correlation

between the two methods show that the Raju-Newman equations may be a valid engineering approximation to the extrapolated crack lengths for this blade. We assume that the Raju-Newman equations are valid for all possible crack lengths and use it to model the SIF in the remainder of this work.

3.2. Simulation 2: Physics-based diagnostics model

Physics-based models are deterministic. By including uncertainties in the model parameters, uncertainty boundaries can be defined for the models' predictions. An example hereof is the natural frequency of a turbomachine blade. Assuming that the length of the blade is an uncertain parameter, the natural frequency can be calculated for various blade lengths to obtain natural frequency boundaries. There are several parameters that can be used as uncertain model parameters in physics-based simulations; however, these parameters must be constrained to values that sensibly contribute the most to changes in the condition indicator. The most researched method for constructing models from uncertain parameters is Monte Carlo based simulations [21], [22]. These simulations construct models from random samples of the uncertain parameters. Monte Carlo models are highly successful but require many samples. Since these physics-based models often need large computational power to evaluate the condition indicator without compromising on numerical accuracy, Monte Carlo methods are infeasible for this application. Other methods such as the unscented transform allow for approximate inference with much fewer model evaluations.

In this work, the unscented transform is used to propagate uncertainties in the inputs to uncertainty in the output of the model. Therefore, a brief background on the unscented transform is provided in this section.

Julier and Jeffrey [23] suggested a strategy for approximating Gaussian probability distributions through non-linear functions. This method, called the unscented transform, is fundamental to the familiar unscented Kalman filter (UKF). The unscented transform approximates a multivariate Gaussian distribution as a set of points called sigma points. Each point has a weight associated with it, so that when the points are processed through a non-linear transformation, a Gaussian distribution is created as the vector function's output. The illustration in Figure 15 (a) was adapted from Ref. [24] and shows the unscented transform as a two-dimensional multivariate Gaussian probability density function. The highlighted region represents one of the contours of the probability density function. In Figure 15 (a) we show that the probability density is distorted when passing it through the non-linear function. A one-dimensional case is also shown in Figure 15 (b).

(a)   (b)
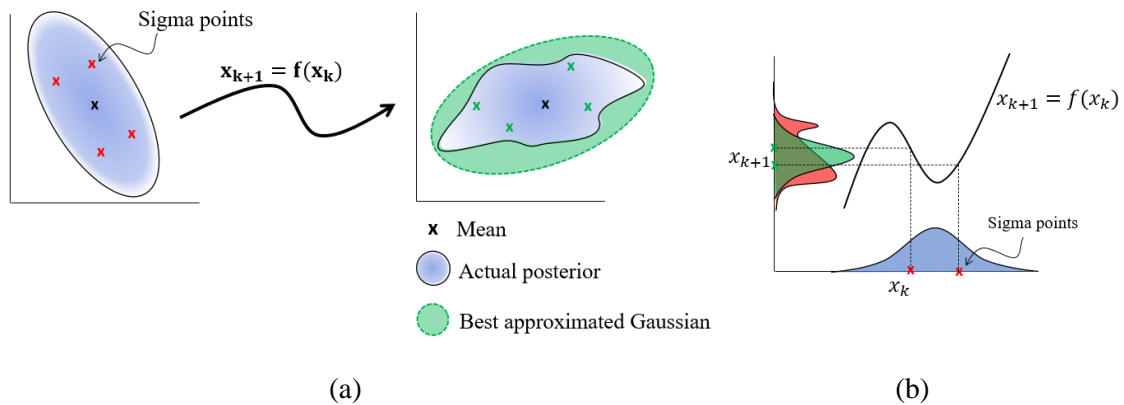
Figure 15: (a) Unscented transform of a multivariate Gaussian distribution adapted from [24] (b) and a one-dimensional illustration of the unscented transform.

The accuracy of the unscented transform depends on the validity of the Gaussian distribution assumption. The unscented transform should provide a computationally cheap approximation to the probability density function if the non-linear function is monotonic and does not generate extreme changes in the function outputs (e.g., lead to a bimodality).

In this work, the unscented transform is used to build a Gaussian physics-based model that captures all the uncertainty of our model parameters. In our case, we would like to find the conditional probability distribution of the form

$$P\left(c|f_{n_0}\right) = \mathcal{N}\left(c \mid \mu\left(f_{n_0}\right), \sigma^2\left(f_{n_0}\right)\right) \tag{5}$$

In other words, the probability distribution across the crack length, c, given the measured natural frequency, f_{n_0}, is modelled as a Gaussian probability density function with a mean, μ, and variance, σ^2. In Section 4 the functions for the mean and variance are derived from data and physics.

It is well accepted that the natural frequency is correlated with the crack length [25]. BTT provides the natural frequency information and therefore we parameterise the mean and variance of the model. As a result, the mean and variance of the estimated Gaussian distribution must be functions of the recorded natural frequency. In the case of this work, we identify the length of the blade and depth of the crack as sensitive parameters for identifying the crack length.

The uncertain parameters are approximated by the bivariate Gaussian distribution

$$\mathcal{N}(\mathbf{x}|\boldsymbol{\mu}, \boldsymbol{\Sigma}) = \mathcal{N}\left(\mathbf{x} \middle| \begin{Bmatrix} \mu_{crack\ depth} \\ \mu_{blade\ length} \end{Bmatrix}, \begin{bmatrix} \sigma^2_{crack\ depth} & 0 \\ 0 & \sigma^2_{blade\ length} \end{bmatrix}\right) \tag{6}$$

where **x** is a two-dimensional vector that contains the crack depth as the first element and the blade length as the second element. As a result, the crack depth has a mean determined from Figure 14 (a) and a variance of $0.01\ mm^2$, while the blade length has a mean of $116\ mm$ and a variance of $1\ mm^2$. The blade length's probability distribution is attributed to the natural variation that occurs during the manufacturing process due to the specified tolerances.

The first mode natural frequency was evaluated from a FEM with different blade lengths and crack depths generated from the unscented transform of the Gaussian distribution in Equation (6). The crack in the blade was modelled by simply tracing out the contour of the crack and separating the top and bottom nodes of the crack face in the FEM. For each simulation, the mesh was refined around the crack front to reduce numerical errors and a refinement convergence tolerance of $0.1\ Hz$ was specified. At regular intervals of crack lengths, the model was evaluated to produce the diagnostics function depicted in Figure 16. The figure also shows where the sigma points of the uncertain parameters were solved. The upper and lower bounds of the 95% confidence interval of the Gaussian probability distribution is shown. No rotational loads were applied to the FEM since the blade is diagnosed at a stationary reference frame (without artificial stiffening). In these physics-based models the known damage is imposed, and the condition indicator is solved. Hence, the model in Figure 16 is inverted such that we can determine the unknown crack length from a measured natural frequency.
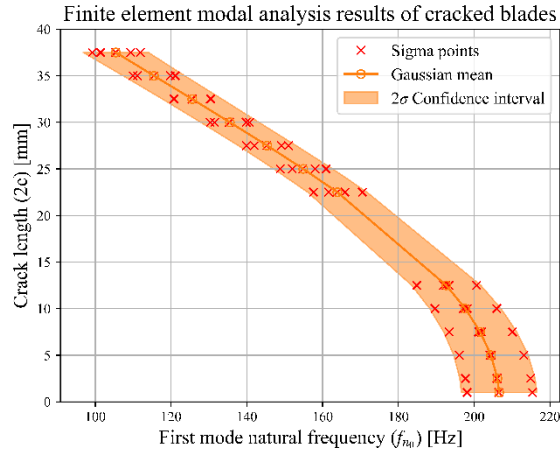
Figure 16: The approximated Gaussian ensemble of possible physics-based diagnostics models that relates the first mode natural frequency to the crack length.

4. Hybrid-based diagnosis

Now that the physics-based diagnostics model has been constructed and experimental data has been collected, an approach for hybrid diagnosis is presented. In Figure 17 we show that we augment the previously defined ensemble-based physics model with the data that was presented in Section 2.2.
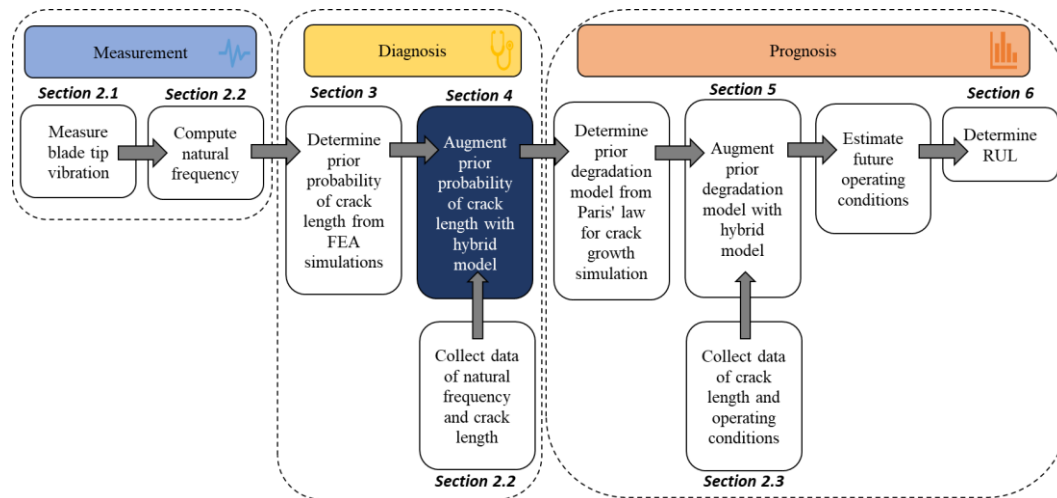
Figure 17: The hybrid framework where the highlighted part shows the hybrid diagnosis stage that is proposed in this section.

There are several methods for combining data with physics-based models to achieve hybrid implementations. Gaussian process regression, deep neural networks, tree-based methods, and support vector regression are examples of data-driven methods that can determine the length of a crack from a blade's natural frequency. One of the best approaches for combining physics-based models with data is Bayesian inference [26]. In Bayesian inference, it is possible to incorporate prior knowledge regarding the model properties (e.g., expected crack length) in the inference process.

A *Gaussian process regression* (GPR) model is an example of a Bayesian inference method that focuses only on the predictive probability distribution

$$P(c^\star | f_n^\star, \boldsymbol{f_n}, \boldsymbol{c}) \tag{7}$$

where we denote the measured natural frequency with $f_n^\star$; the crack length, inferred with the process described in Section 3.2, with $c^\star$; and the N-sized historical natural frequency and crack length parameters, obtained after N-NDT inspections, with $\boldsymbol{f_n} \in \mathbb{R}^N$ and $c \in \mathbb{R}^N$ respectively. Hence, we model the probability distribution over the crack length conditioned on the natural frequency of the current blade under consideration and all the historical data using the GPR.

GPR is useful for hybrid diagnosis of the crack length in a turbomachine rotor blade for the following reasons [26]:

1. GPR is an analytical closed form solution to Bayesian inference. With the appropriate choice of a kernel, it is possible to select a near infinite number of functions to fit the data and obtain a tractable solution to the predictive probability distribution. Overfitting of GPR models is treated by selecting appropriate prior models (specifying the kernel functions and identifying appropriate parameters) that fit the data.
2. GPR is a non-parametric model that does not limit the model to a specific assumption about the relationship between natural frequency and crack length; instead, the choice of a covariance function expresses a wide range of hypotheses that are marginalised through exact integration to find the models that best suit the data.
3. One of the largest drawbacks is that the computational complexity of complete inference is $\mathcal{O}(N^3)$ for GPR models, where N represents the number of observations. However, the computational cost will remain low if the GPR model is used in a hybrid framework with limited representative data.

GPR use an input dependent covariance function to model the predictive distribution. A common covariance function is the squared exponential kernel

$$k(f_n, f_n') = \sigma_i^2 \exp\left(-\frac{(f_n - f_n')^2}{2\ell^2}\right) \tag{8}$$

The model hyperparameters σ_i^2 and ℓ^2 are parameters that are optimised by selecting model parameters that maximise the marginal likelihood, namely $P(\boldsymbol{f_n} | \mathbf{c}, \sigma_i^2, \ell^2)$. The squared exponential kernel is a stationary covariance function, meaning the model is locally influenced by the data and is not expected to have predictive characteristics [27]. $\mathbf{K}$ denotes the matrix function that arises when evaluating the squared exponential kernel at the input vectors. The joint prior probability distribution of the function over $\boldsymbol{c}$ and $c^\star$,

$$\mathrm{P}\left(\left\{\begin{matrix} \boldsymbol{c} \\ c^\star \end{matrix}\right\}\right) = \mathcal{N}\left(\left\{\begin{matrix} \boldsymbol{c} \\ c^\star \end{matrix}\right\} \middle| \left\{\begin{matrix} m(\boldsymbol{f_n}) \\ m(f_n^\star) \end{matrix}\right\}, \begin{bmatrix} \mathbf{K}(\boldsymbol{f_n}, \boldsymbol{f_n}) & \mathbf{K}(\boldsymbol{f_n}, f_n^\star) \\ \mathbf{K}(f_n^\star, \boldsymbol{f_n}) & \mathbf{K}(f_n^\star, f_n^\star) \end{bmatrix}\right) \tag{9}$$

is a joint multivariate Gaussian distribution with a mean vector function $\mathbf{m}(\boldsymbol{f_n})$, and a covariance matrix function $\mathbf{K}(\boldsymbol{f_n}, \boldsymbol{f_n})$. Both the mean and covariance functions are defined for all inputs of the historical recorded natural frequencies. In Equation (9), $\mathbf{m}(f_n^\star)$ and $\mathbf{K}(f_n^\star, f_n^\star)$ are defined for all inputs we wish to interrogate. Solving the GPR model allows us to compute the posterior multivariate Gaussian distribution

$$\mathcal{N}(c^\star | \boldsymbol{\mu}, \boldsymbol{\Sigma}) = \mathcal{N}(f_n^\star | \mathbf{K}(f_n^\star, \boldsymbol{f_n}) \left(\mathbf{K}(\boldsymbol{f_n}, \boldsymbol{f_n})\right)^{-1} \left(\mathbf{c} - \mathbf{m}(\boldsymbol{f_n})\right) + \mathbf{m}(f_n^\star),$$
$$\mathbf{K}(f_n^\star, f_n^\star) - \mathbf{K}(f_n^\star, \boldsymbol{f_n})(\mathbf{K}(\boldsymbol{f_n}, \boldsymbol{f_n}))^{-1}\mathbf{K}(\boldsymbol{f_n}, f_n^\star)) \tag{10}$$

GPR conventionally solves the predictive distribution from a zero mean Gaussian prior distribution ($\mathbf{m}(\boldsymbol{f_n}) = \mathbf{0}$) [27], [28]. This is due to a lack of prior understanding of the function's

structure. The conventional GPR method was applied to the data and is presented in Figure 18 (a). The figure shows the data points with the mean and 2σ confidence interval shaded in blue. The physics-based model is also plotted for comparison. The prior distribution of the function has a zero mean and a constant standard deviation due to the selected squared exponential kernel. Since this model only relies on the data, it is considered a data-driven model. The model presented in Figure 18 (b), on the other hand, shows the hybrid-based model and incorporates the mean and variance function of the prior physics-based model derived in Section 3. That is the mean vector function $\mathbf{m}(f_n)$ and the covariance matrix $\mathbf{K}(f_n, f_n)$ are equated to the model in Figure 16.
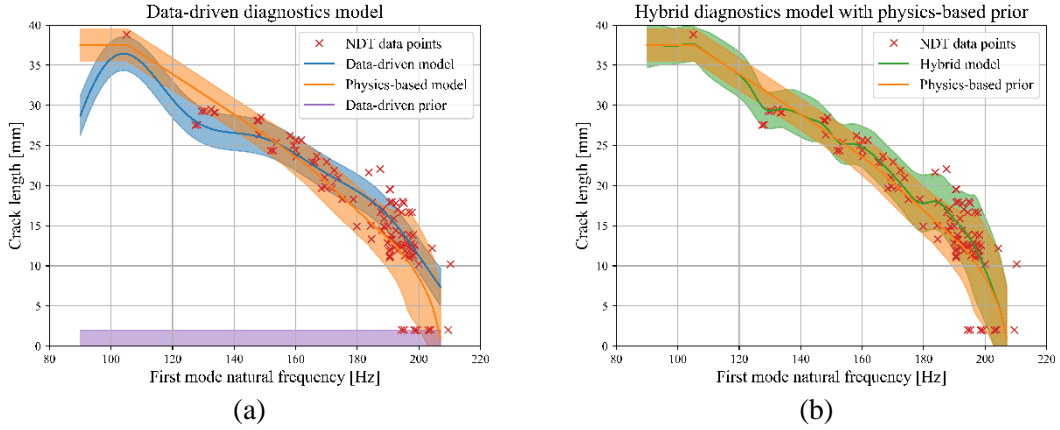
Figure 18: (a) A GPR regression model applied only to the experimental data with a zero-mean prior compared to the physics-based model and (b) a GPR regression model that uses the physics-based model as a prior to represent a hybrid-based approach to diagnosis.

Figure 18 highlights the benefits of the suggested hybrid methodology. The physics-based model deviates slightly from the measured data. This can potentially be attributed to model discrepancy, input uncertainties, etc. In contrast, the data-driven model, which uses a zero-mean prior, tends towards zero in regions where data was not collected. This behaviour is non-physical and therefore could lead to erroneous predictions. This key difference highlights the importance of hybrid methods when limited data is available. The physics-based model is used as a prior in the proposed hybrid approach and acts as regularisation to ensure that the behaviour of the hybrid model is physical in regions where historical collected NDT data is scarce. As shown, the data driven technique requires much more data to be implemented for diagnosis.

To further illustrate this point, a five-fold leave-one-out cross-validation (LOOCV) method was used in the validation procedure. This approach divides the data into five equal parts, trains the model on four of them, then calculates the root mean squared error (RMSE) between the model predicted value and the observations using the fifth division as validation data. We considered the following set of models for comparison:

1. The physics-based model derived in Section 3.
2. The Gaussian process regression model with a squared exponential kernel. The hyperparameters of the squared exponential kernel are optimised with respect to the marginal likelihood of the training data.
3. A random forest tree-based method with a maximum depth of 2.
4. A support vector regression with a squared exponential kernel. The hyperparameter of the radial-basis function kernel are also optimised with respect to the marginal likelihood of the training data in a similar procedure as the GPR model.

5. A multilayer perceptron with 20 latent variables in the first hidden layer and 10 in the second hidden layer and rectified linear activation functions [29].

6. The hybrid method proposed in Section 4.

The five-fold LOOCV was performed 100 times to evaluate the performance of each model. The models were initialised with different starting points during each run. This randomisation process ensures that the validation investigation is unbiased towards the data as well as the model's initialisation. The results of the mean and standard deviation of the RMSE of all model types are tabulated in Table 1. In the table's final row, we use summary statistics to estimate the percentages of the times that any of the model types has a lower RMSE than the hybrid technique (given a random set of training data). The random forest was the best of the data-driven models, but in more than 91% of the validation trials, the hybrid model's RMSE surpassed the random forest's RMSE. The results highlight two important points:

- Hybrid models are important for applications where historical NDT fault data is scarce.
- There are other potential data-driven models that can further improve the performance of the proposed hybrid framework (e.g., the GPR data-driven model performed second best of the data-driven models). Investigating further improvements are outside the scope of this work.

Table 1: Average five-fold cross-validation RMS error of the different model types for 100 random initialisation training repeats

		Physics-based method	GPR	Random forest	Support vector regression	Neural network	Hybrid method
LOOCV 100 repeats	**RMSE Mean**	2.8643	2.022	1.9666	2.1259	2.2448	1.725
	RMSE Standard deviation	0.0	0.0999	0.1284	0.049	0.1699	0.1189
Percentage of times that the $RMSE_{model} < RMSE_{hybrid}$		0.00%	2.79%	8.37%	0.09%	0.6 %	-

5. Hybrid based prediction of crack growth rate

We now demonstrate the hybrid degradation model highlighted in Figure 19. In this section we utilise the data collected in Section 3.3, the hybrid diagnostics model derived in Section 5 and Paris' law to infer the current crack length and the probability density function of the Paris law coefficients.
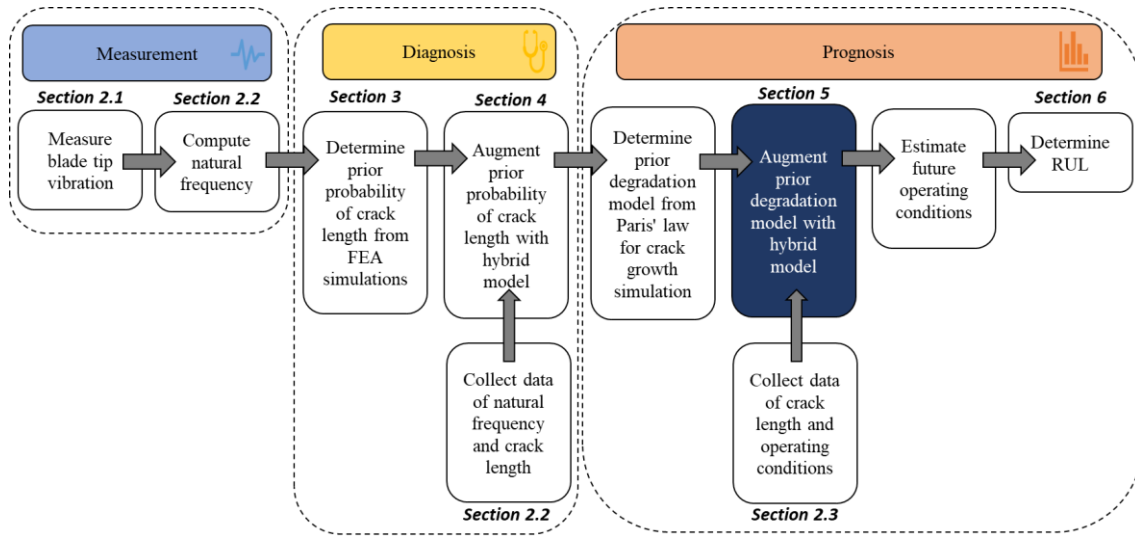
Figure 19: The hybrid framework where the highlighted part shows the hybrid degradation model that is presented in this section.

Coppe et al. [30], [31] first investigated models of uncertain Paris' law coefficients for RUL prediction. We propose a similar approach to these models however we incorporate the use of regular uncertain condition monitoring estimates of the current crack length. A hidden Markov chain model is proposed for treating uncertainty in the crack growth. The hidden Markov chain model treats the crack length and the Paris law coefficients as hidden latent variables that follow a Markov process. A noisy estimation of the crack length was observed at regular intervals when BTT condition monitoring tests were conducted. The mean and variance of this estimation are determined from the diagnosis model in Figure 18 (b). The unobserved crack length changes according to Paris' law whereas the Paris law coefficients remain constant. It has become standard practice in condition monitoring to use Bayesian filtering methods to solve the posterior distribution of the state-of-health for condition indicators [21].

Gathering measurement samples, from BTT tests, and predicting the hidden crack length allows us to compute the posterior probability distribution of the crack length given all the observations and future operating conditions. The posterior distribution of the hidden state vector is of great importance, because all the parameters of the hidden state are essential in predicting RUL (RUL is a function of the crack length and Paris law coefficients) [3], [32]. Continuing our use of the unscented transform, we evaluate this posterior distribution using the *unscented Kalman filter* (UKF). The UKF approximates the hidden state vector as a multivariate Gaussian distribution but allows for nonlinear transition functions which the traditional Kalman filter fails to model.

The UKF was applied to the measured natural frequencies obtained from the BTT experiments. Two models are proposed namely (i) a *physics -diagnostics-prognostics* model and (ii) a *hybrid-diagnosis-prognostics* model. The *physics-diagnostics-prognostics* model only uses the BTT natural frequencies and the model in Figure 16 as the observations for the UKF. The state transition function is derived from Paris law with constant coefficients. The *hybrid-diagnosis-prognosis* model, alternatively, uses (i) the collected diagnostics data, (ii) the BTT natural frequency and (iii) the model in Figure 18 (b) as observations. Although the state vector of this UKF includes the Paris law coefficients, the transition function is constant for these parameters. Table 2 summarises the two UKF models. The prior distribution of the Paris' law coefficients we determined from literature for the specific material [33]–[35].

20

Table 2: UKF model comparison for physics-based and data-driven models

	Physics-based-diagnostics-physics-based-prognostics	Hybrid-diagnosis-hybrid-prognostics
State vector	Crack length.	Crack length and Paris law coefficients (C and m).
Prior mean vector	$\{a_0\} = \{0.1\}$	$\begin{Bmatrix} a_0 \\ C_0 \\ m_0 \end{Bmatrix} = \begin{Bmatrix} 0.1 \\ 2.136 \times 10^{-10} \\ 2.612 \end{Bmatrix}$
Prior covariance matrix	$\Sigma_0 = [1]$	$\Sigma_0 = \begin{bmatrix} 1 & 0 & 0 \\ 0 & 8.08 \times 10^{-11} & 0 \\ 0 & 0 & 0.069 \end{bmatrix}$
Measurement	Evaluate physics-based model at measured BTT natural frequency to estimate the crack length.	Evaluate hybrid GPR model at estimated BTT natural frequency to infer the crack length.
Measurement noise	Physics-based diagnostics model uncertainty.	Hybrid diagnostics model uncertainty.
Transition	Known nominal stress amplitude and number of cycles are used in the integrated Paris law with constant coefficients to predict the crack length transition.	Known nominal stress amplitude and number of cycles are used in integrated Paris law with coefficients in state vector. Coefficients in state vector are kept constant, while the crack length is updated.
Transition noise	Constant noise of $0.1\ mm$ variance. See Section 3.1	Constant noise of $0.1\ mm$ variance of crack length with zero noise for Paris law coefficients. See Section 3.1

Figure 20 presents the measured crack lengths and number of cycles for all 10 blades used in our experiments. The crack length estimates of the two UKF models are also presented. It is evident that the hybrid UKF is closer to the true measurements and is therefore better.
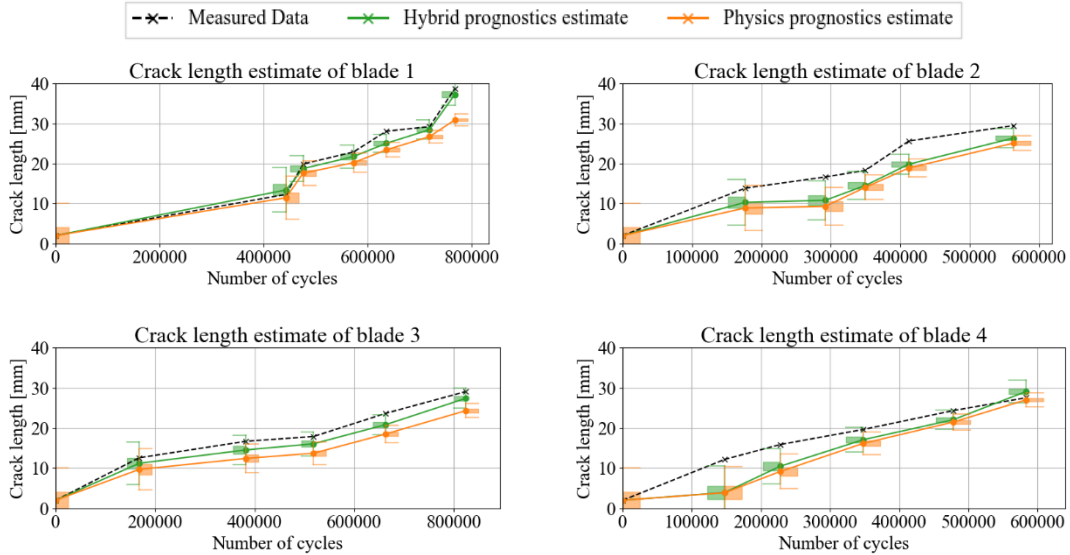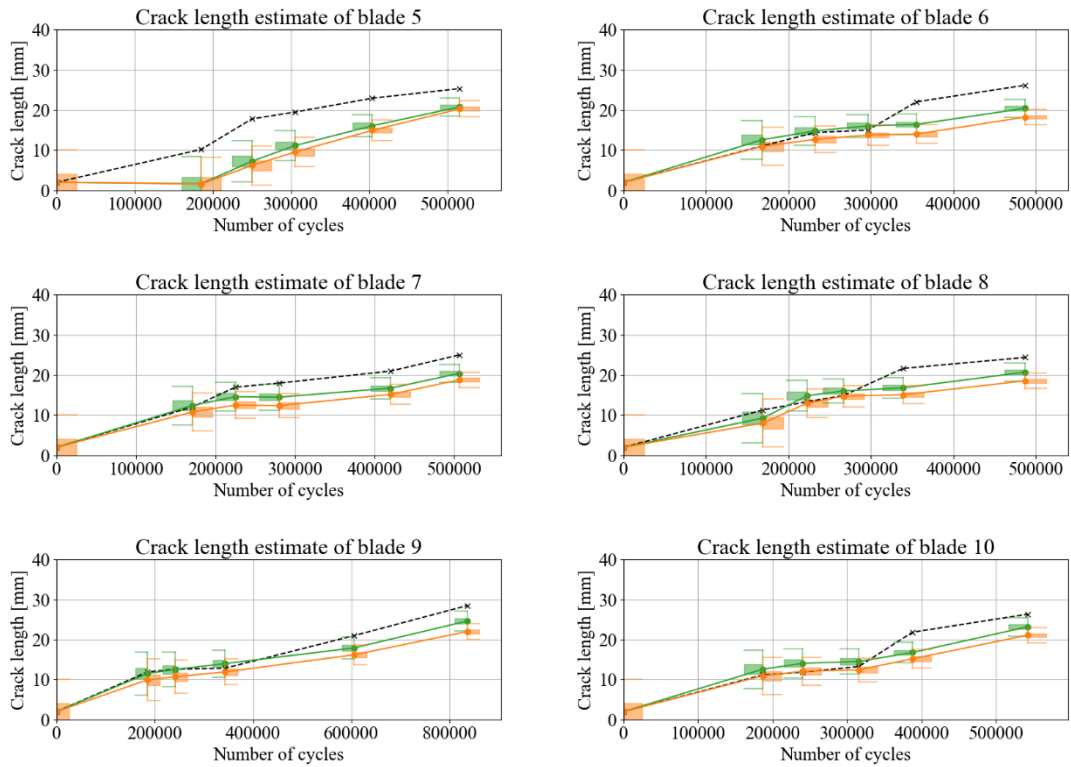
Figure 20: UKF estimations of crack length from hybrid-diagnostics-hybrid-prognostics model (green) and physics-based-diagnostics-physics-based-prognostics model (orange).

The updated Paris law coefficients are shown in Figure 21 with the prior 95% confidence interval (CI). The Paris law coefficients are given a Gaussian prior with the same covariances as the prior of the hybrid technique when using the physics-based model for prediction. This is to overcome the deterministic nature of Paris' law and to compare the ensemble-based techniques.
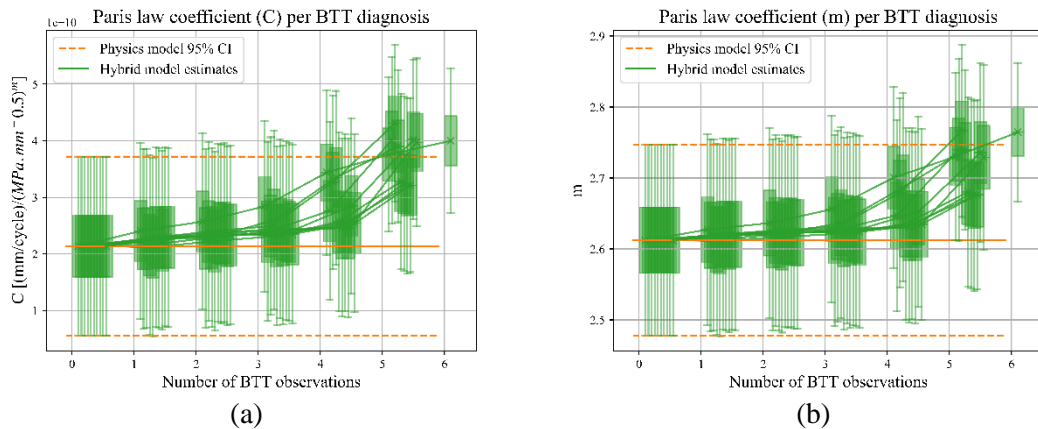
Figure 21: Posterior estimates of Paris law coefficients obtained from UKF of (a) constant C and (b) exponent m as a function of the number of BTT tests for a single blade.

6. Estimating remaining useful life

Ultimately the models derived in the previous sections need to be combined to determine the RUL of the turbomachine rotor blade. The hybrid UKF model consists of all the parameters needed to predict the RUL of the blade when assuming the future operating conditions (nominal stress amplitude and number of cycles) and the maximum allowable crack length. In the case of these experiments, we chose to evaluate the model performance by predicting the number of cycles required to reach the final measured crack length of each blade. Samples from the posterior distribution is used for predicting RUL. We determine the RUL from an unscented transformation of the multivariate Gaussian probability distribution consisting of the current crack length and the Paris law coefficients used in Section 5. Each sigma point was used to predict the RUL and finally the RUL probability density function. The RUL estimates of both the hybrid and data-driven methods are tabulated in Table 3. Figure 22 presents box plots of the RUL estimations from both UKF models at the BTT measurement intervals. The precision and accuracy of the model at each BTT measurement interval are plotted in Figure 23 (a) and (b) respectively. It is evident that with each condition monitoring interval the RUL estimate becomes more precise and less uncertain. The figure indicates that both the physics-based and hybrid-based prognostics models have super linear convergence rates to the true RUL. This is an expected result since each BTT measurement provides evidence of the current crack length. The hybrid model is also shown to outperform its physics-based counterpart, since the absolute error and standard deviation decreases faster for each BTT condition monitoring interval.

Table 3: Remaining useful life estimation from hybrid and physics-based methods for all blades.

| Blade	True RUL	Hybrid-based method		Physics-based method	
		Mean	Standard deviation	Mean	Standard deviation
1	7,678E+05	1,485E+06	6,642E+05	1,485E+06	6,642E+05
	3,248E+05	6,666E+05	2,289E+05	8,740E+05	3,316E+05
	2,918E+05	3,715E+05	6,420E+04	4,686E+05	1,475E+05
	1,951E+05	2,660E+05	4,034E+04	3,661E+05	1,164E+05
	1,320E+05	1,550E+05	1,223E+04	2,371E+05	6,493E+04
	4,874E+04	5,249E+04	7,024E+03	1,080E+05	4,119E+04
	0,000E+00	4,740E+02	4,155E+02	2,860E+04	1,811E+04
2	5,628E+05	1,356E+06	6,313E+05	1,356E+06	6,313E+05
	3,862E+05	7,159E+05	2,256E+05	8,069E+05	2,956E+05
	2,709E+05	6,519E+05	2,009E+05	8,213E+05	3,403E+05
	2,131E+05	4,207E+05	1,180E+05	4,956E+05	1,839E+05
	1,503E+05	2,136E+05	3,889E+04	2,880E+05	9,576E+04
	0,000E+00	7,571E+03	3,955E+03	4,571E+04	2,910E+04
3	8,244E+05	1,524E+06	6,396E+05	1,524E+06	6,396E+05
	6,563E+05	1,014E+06	1,821E+05	1,198E+06	3,738E+05
	4,422E+05	6,501E+05	1,185E+05	8,066E+05	2,393E+05
	3,061E+05	4,402E+05	7,703E+04	5,848E+05	1,849E+05
	1,616E+05	1,990E+05	1,940E+04	3,254E+05	1,103E+05
	0,000E+00	3,334E+03	2,402E+03	5,254E+04	3,331E+04
4	5,831E+05	1,365E+06	6,168E+05	1,365E+06	6,168E+05
	4,354E+05	1,426E+06	7,960E+05	1,451E+06	7,819E+05
	3,551E+05	7,021E+05	1,878E+05	8,354E+05	3,224E+05
	2,351E+05	3,330E+05	6,203E+04	4,103E+05	1,236E+05
	1,050E+05	1,199E+05	1,278E+04	1,751E+05	5,389E+04
	0,000E+00	-2,943E+03	1,916E+03	5,702E+03	6,308E+03
5	5,153E+05	1,274E+06	5,945E+05	1,274E+06	5,945E+05
	3,303E+05	1,628E+06	9,606E+05	1,615E+06	9,144E+05
	2,654E+05	8,011E+05	3,213E+05	9,296E+05	4,272E+05
	1,116E+05	2,325E+05	6,235E+04	3,219E+05	1,423E+05
	0,000E+00	2,909E+04	1,348E+04	7,946E+04	5,032E+04
6	4,874E+05	1,264E+06	6,054E+05	1,264E+06	6,054E+05
	3,191E+05	5,514E+05	1,504E+05	6,493E+05	2,260E+05
	2,552E+05	4,612E+05	1,310E+05	6,118E+05	2,414E+05
	1,912E+05	3,459E+05	9,034E+04	4,881E+05	2,135E+05
	1,322E+05	2,590E+05	6,784E+04	3,849E+05	1,710E+05
	0,000E+00	3,659E+04	1,639E+04	1,307E+05	8,191E+04
7	5,062E+05	1,292E+06	6,090E+05	1,292E+06	6,090E+05
	3,353E+05	5,510E+05	1,400E+05	6,566E+05	2,354E+05
	2,811E+05	4,647E+05	1,105E+05	6,040E+05	2,129E+05
	2,263E+05	4,099E+05	9,938E+04	5,632E+05	2,290E+05
	8,597E+04	1,910E+05	5,599E+04	2,944E+05	1,405E+05
	0,000E+00	3,164E+04	1,468E+04	1,045E+05	6,576E+04
8	4,873E+05	1,292E+06	6,139E+05	1,292E+06	6,139E+05
	3,184E+05	6,529E+05	2,183E+05	7,428E+05	2,730E+05
	2,650E+05	4,361E+05	9,923E+04	5,447E+05	1,953E+05
	2,207E+05	3,457E+05	7,277E+04	4,233E+05	1,222E+05
	1,485E+05	2,522E+05	5,963E+04	3,400E+05	1,334E+05
	0,000E+00	2,548E+04	1,261E+04	1,013E+05	6,380E+04
9	8,359E+05	1,479E+06	6,120E+05	1,479E+06	6,120E+05
	6,507E+05	8,912E+05	1,706E+05	1,029E+06	2,801E+05
	5,951E+05	9,061E+05	1,830E+05	1,014E+06	2,835E+05
	4,928E+05	7,041E+05	1,146E+05	8,703E+05	2,485E+05
	2,299E+05	3,147E+05	4,559E+04	4,420E+05	1,257E+05
	0,000E+00	1,087E+04	5,241E+03	8,264E+04	5,208E+04
10	5,421E+05	1,344E+06	6,209E+05	1,344E+06	6,209E+05
	3,552E+05	5,820E+05	1,534E+05	6,869E+05	2,180E+05
	3,020E+05	5,172E+05	1,097E+05	6,657E+05	2,613E+05
	2,267E+05	4,253E+05	1,276E+05	5,618E+05	2,276E+05
	1,543E+05	2,569E+05	6,289E+04	3,528E+05	1,337E+05
	0,000E+00	1,127E+04	5,662E+03	7,624E+04	4,818E+04

Since all blades are plotted together in Figure 23 (a) and (b) it may not be evident that the hybrid model is more accurate than the physics-based method. Therefore, we define the relative accuracy

$$Relative\ accuracy = \frac{\left|RUL_{physics} - RUL_{true}\right| - \left|RUL_{hybrid} - RUL_{true}\right|}{\left|RUL_{physics} - RUL_{true}\right|} \quad (11)$$

and relative precision metrics

$$Relative\ precision = \frac{\sigma_{hybrid} - \sigma_{physics}}{\sigma_{physics}} \quad (12)$$

and plot them in Figure 24 (a) and (b) respectively. The figure shows that the hybrid model can predict the RUL with an average improvement of at least 80% while reducing the average model uncertainty at least 85% after five BTT condition monitoring measurements. We identify that there was no improvement for two of the blades when at least two BTT tests were conducted, however after the five BTT tests an improvement of at least 60% was shown.
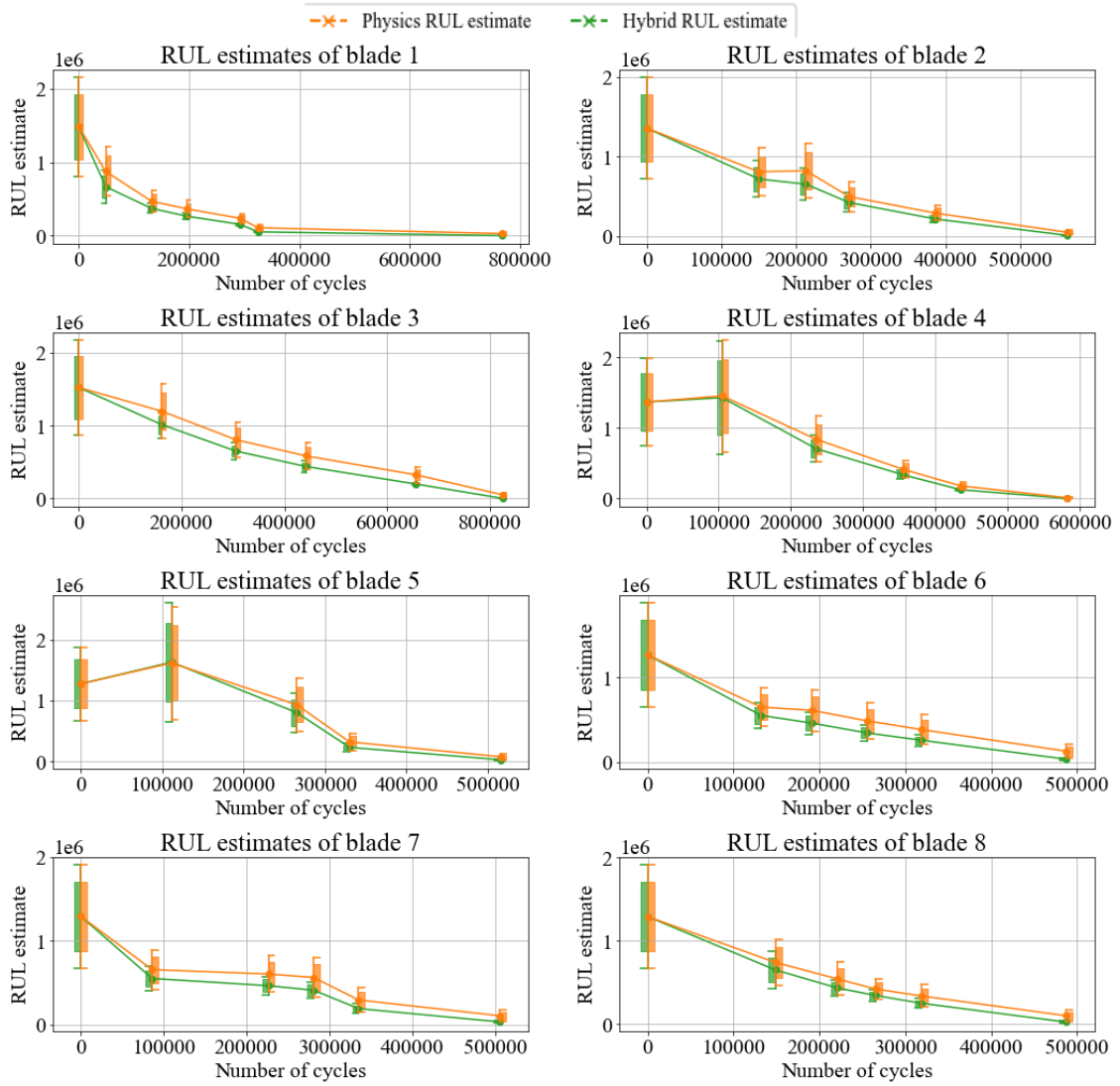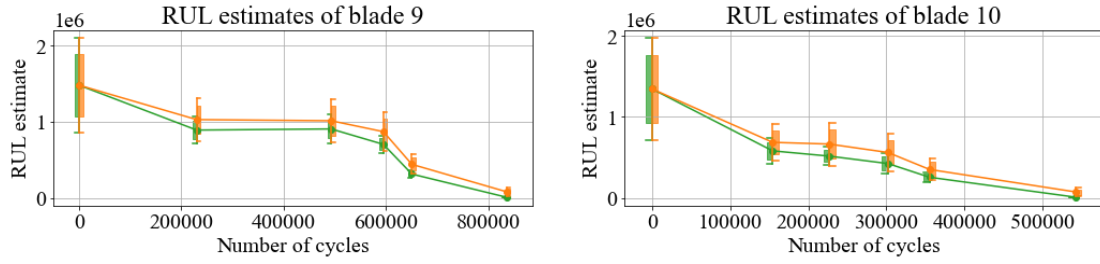
**Figure 22: RUL for all 10 blades estimated from UKF posterior probability density function based on hybrid-diagnostics-hybrid-prognostics model (green) and physics-based-diagnostics-physics-based-prognostics model (orange).**

(a)   (b)
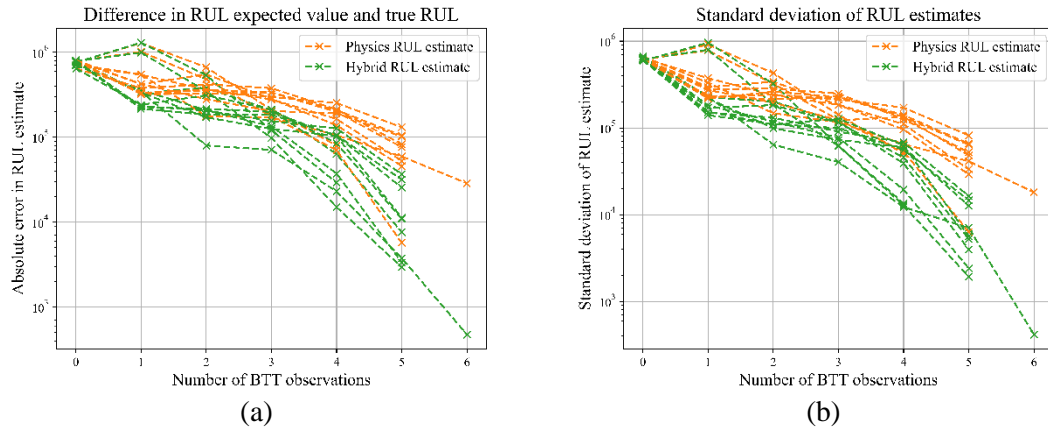
Figure 23: (a) Precision of RUL estimates relative to the true measured RUL as a function of the number of BTT tests and (b) the uncertainty of the RUL estimates.

(a)   (b)
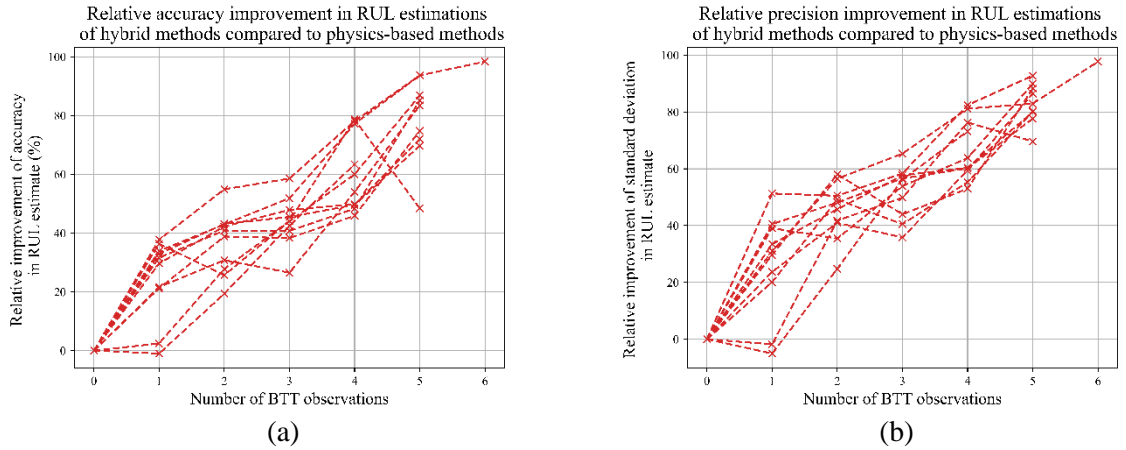
Figure 24: (a) Relative accuracy improvement and (b) relative precision improvement of hybrid RUL estimation compared to physics-based methods.

7. Conclusion

In this article we proposed a novel hybrid framework for determining RUL of mechanical components. These components have partially observable damage states that can be monitored

25

through routine inspections to accumulate NDT data. We identified an opportunity for demonstrating the hybrid method on fatigue cracks in turbomachine rotor blades.

We highlight the use of BTT as a condition monitoring technique for turbomachine rotor blades. An LSSA method was implemented on the BTT measurements of 10 blades, with varying crack lengths, to estimate the stationary referenced natural frequency of the blade. Experimental results showed that the natural frequency was estimated within 10 *Hz* from the measured natural frequency of modal impact hammer tests. A novel hybrid implementation of a GPR model was used to diagnose cracks in the blade from a physics-based prior model constructed from FEM simulations. The hybrid-based diagnostics model was shown to improve the physics-based model by reducing the model uncertainty near the measured diagnostics data points. It was shown that using a GPR model without a physics-based prior and limited data resulted in inaccurate diagnosis of the crack length from the measured natural frequency. A further investigation highlighted that data-driven techniques are not as effective as hybrid diagnosis methods when limited data are available. Subsequently, we proposed a hybrid prognostics model in the form of a UKF that treats the current damage and crack growth rate parameters as hidden state parameters. It was shown that the hybrid implementation had increased precision and accuracy of the RUL when trying to predict the number of cycles until the last measured crack length of the blade is reached.

From the results we conclude that the hybrid implementation, indeed, improves the accuracy and precision of predicting RUL for turbomachine rotor blades. This highlights that hybrid methods are essential for remaining useful life estimation in practical circumstances where limited data is available.

References

[1]   A. Saxena, "Conference Slides: Prognostics Tutorial," in *Annual Conference of the PHM Society (PHM2010)*, 2010.

[2]   K. Kai Goebel, A. Abhinav Saxena, S. Sankalita Saha, B. Bhaskar Saha, and J. Jose Celaya, "Prognostic performance metrics," in *Machine Learning and Knowledge Discovery for Engineering Systems Health Management*, 2011, pp. 149–171.

[3]   A. Cubillo, S. Perinpanayagam, and M. Esperon-Miguez, "A review of physics-based models in prognostics: Application to gears and bearings of rotating machinery," *Advances in Mechanical Engineering*, vol. 8, no. 8, pp. 1–21, 2016.

[4]   Y. Lei, N. Li, L. Guo, N. Li, T. Yan, and J. Lin, "Machinery health prognostics: A systematic review from data acquisition to RUL prediction," *Mechanical Systems and Signal Processing*, vol. 104, pp. 799–834, 2018.

[5]   D. An, N. H. Kim, and J. H. Choi, "Practical options for selecting data-driven or physics-based prognostics algorithms with reviews," *Reliability Engineering and System Safety*, vol. 133, pp. 223–236, 2015.

[6]   L. Liao and F. Köttig, "Review of hybrid prognostics approaches for remaining useful life prediction of engineered systems, and an application to battery life prediction," *IEEE Transactions on Reliability*, vol. 63, no. 1, pp. 191–207, 2014.

[7]   "ISO 13381-1," *Condition monitoring and diagnostics of machines — Prognostics — Part 1: General guidelines*, 2015.

[8]   J. C. P. Brits, "An experimental and stochastic approach to estimate the fatigue crack life of a turbomachinery blade using finite element modelling," University of Pretoria, 2016.

[9]   D. H. Diamond, "A probabilistic approach to blade tip timing data processing," University

of Pretoria, 2016.

[10] M. Mohamed, P. Bonello, and P. Russhard, "A novel method for the determination of the change in blade tip timing probe sensing position due to steady movements," *Mechanical Systems and Signal Processing*, vol. 126, pp. 686–710, 2019.

[11] L. Biggio and I. Kastanis, "Prognostics and health management of industrial assets: Current progress and road ahead," *Frontiers in Artificial Intelligence*, 2020.

[12] F. Jia, Y. Lei, J. Lin, X. Zhou, and N. Lu, "Deep neural networks: A promising tool for fault characteristic mining and intelligent diagnosis of rotating machinery with massive data," *Mechanical Systems and Signal Processing*, vol. 72–73, pp. 303–315, 2016.

[13] K. Chen, W. Wang, X. Zhang, and Y. Zhang, "New step to improve the accuracy of blade tip timing method without once per revolution," *Mechanical Systems and Signal Processing*, vol. 134, p. 106321, Dec. 2019.

[14] J. L. Meriam, L. G. Kraige, and J. N. Bolton, *Engineering Mechanics: Dynamics, 9th Edition*. 2018.

[15] D. H. Diamond, P. S. Heyns, and A. J. Oberholster, "Improved blade tip timing measurements during transient conditions using a state space model," *Mechanical Systems and Signal Processing*, vol. 122, pp. 555–579, 2019.

[16] J. T. VanderPlas, "Understanding the Lomb–Scargle periodogram," *The Astrophysical Journal Supplement Series*, vol. 236, no. 1, p. 16, May 2018.

[17] J. Gallego-Garrido, G. Dimitriadis, and J. R. Wright, "A Class of Methods for the Analysis of Blade Tip Timing Data from Bladed Assemblies Undergoing Simultaneous Resonances—Part I: Theoretical Development," *International Journal of Rotating Machinery*, vol. 2007, pp. 1–11, 2007.

[18] L. Witek, "Simulation of crack growth in the compressor blade subjected to resonant vibration using hybrid method," *Engineering Failure Analysis*, vol. 49, pp. 57–66, 2015.

[19] J. C. Newman and I. S. Raju, "An empirical stress-intensity factor equation for the surface crack," *Engineering Fracture Mechanics*, vol. 15, no. 1–2, pp. 185–192, 1981.

[20] J. C. Raju and I. S. Newman, "Stress intensity factor equations for cracks in three-dimensional bodies subjected to tension and bending loads," *NASA Technical meomorandum*, no. May, 1984.

[21] M. Corbetta, C. Sbarufatti, M. Giglio, and M. D. Todd, "Optimization of nonlinear, non-Gaussian Bayesian filtering for diagnosis and prognosis of monotonic degradation processes," *Mechanical Systems and Signal Processing*, vol. 104, pp. 305–322, 2018.

[22] P. Baraldi, F. Cadini, F. Mangili, and E. Zio, "Prognostics under different available information," *Chemical Engineering Transactions*, vol. 33, pp. 163–168, 2013.

[23] S. J. Julier and U. K. Jeffrey, "A new extension of the Kalman filter to nonlinear systems," *AeroSense'97. International Society for Optics and Photonics*, pp. 182–193, 1997.

[24] H. Singh, "The Unscented Kalman Filter: Anything EKF can do I can do it better!," *Towards Data Science*, 2018. [Online]. Available: https://towardsdatascience.com/the-unscented-kalman-filter-anything-ekf-can-do-i-can-do-it-better-ce7c773cf88d. [Accessed: 21-Oct-2019].

[25] M. Elshamy, W. A. Crosby, and M. Elhadary, "Crack detection of cantilever beam by natural frequency tracking using experimental and finite element analysis," *Alexandria Engineering Journal*, vol. 57, no. 4, pp. 3755–3766, 2018.

[26] C. M. Bishop, *Pattern recognition and machine learning*. Springer, 2006.

[27]   D. K. Duvenaud, "Automatic Model Construction with Gaussian Processes," University of Cambridge, 2014.

[28]   C. E. Rasmussen and C. K. I. Wiliams, *Gaussian Processes for Machine Learning*. 2006.

[29]   A. F. Agarap, "Deep Learning using Rectified Linear Units (ReLU)," 2018.

[30]   A. Coppe, M. J. Pais, R. T. Haftka, and N. H. Kim, "Using a simple crack growth model in predicting remaining useful life," *Journal of Aircraft*, vol. 49, no. 6, pp. 1965–1973, 2012.

[31]   A. Coppe, R. T. Haftka, N. H. Kim, and F. G. Yuan, "Uncertainty reduction of damage growth properties using structural health monitoring," *Journal of Aircraft*, vol. 47, no. 6, pp. 2030–2038, 2010.

[32]   M. Jouin, R. Gouriveau, D. Hissel, M. C. Péra, and N. Zerhouni, "Particle filter-based prognostics: Review, discussion and perspectives," *Mechanical Systems and Signal Processing*, vol. 72, pp. 2–31, 2016.

[33]   W. Wang, W. Hu, and N. Armstrong, "Fatigue crack prognosis using Bayesian probabilistic modelling," *Mechanical Engineering Journal*, vol. 4, no. 5, pp. 16-00702-16–00702, 2017.

[34]   G. Mrowka-Nowotnik, J. Sieniawski, and A. Nowotnik, "Tensile properties and fracture toughness of heat treated 6082 alloy," *Journal of Achievements in Materials and Manufacturing Engineering (JAMME)*, vol. 17, no. 1–2, pp. 105–108, 2006.

[35]   W. F. Wu and C. C. Ni, "Statistical aspects of some fatigue crack growth data," *11th International Conference on Fracture 2005, ICF11*, vol. 8, pp. 5801–5806, 2005.

B Ellis: Conceptualization, Methodology, Software, Validation, Formal analysis, Investigation, Resources, Writing - Original Draft, Visualization **P Stephan Heyns:** Supervision, Writing - Review & Editing **S Schmidt:** Supervision, Writing - Review & Editing

Declaration of interests

☒The authors declare that they have no known competing financial interests or personal relationships that could have appeared to influence the work reported in this paper.

☐The authors declare the following financial interests/personal relationships which may be considered as potential competing interests: